Inorganic Chemistry

Article

pubs.acs.org/IC

Magnetic Interactions in a Series of Homodinuclear Lanthanide Complexes

Peter Comba,*[,†] Michael Großhauser,[†] Rüdiger Klingeler,[‡] Changhyun Koo,[‡] Yanhua Lan,[§,∥] Dennis Müller,[†] Jaena Park,[‡] Annie Powell,[§,∥] Mark J. Riley,[⊥] and Hubert Wadepohl[†]

[†]Anorganisch-Chemisches Institut und Interdisziplinäres Zentrum für Wissenschaftliches Rechnen (IWR), Universität Heidelberg, INF 270, D-69120 Heidelberg, Germany

[‡]Kirchhoff-Institut für Physik, Universität Heidelberg, INF 227, D-69120 Heidelberg, Germany

[§]Institut für Anorganische Chemie, Karlsruhe Institute of Technology (KIT), Engesserstrasse 15, Geb. 30.45, D-76131 Karlsruhe, Germany

[∥]Institute of Nanotechnology (INT), P.O. Box 3640, D-76021 Karlsruhe, Germany

[⊥]School of Chemistry and Molecular Biosciences, University of Queensland, Brisbane, Queensland 4072, Australia

S *Supporting Information*

ABSTRACT: A series of seven isostructural homodinuclear lanthanide complexes are reported. The magnetic properties (ac and dc SQUID measurements) are discussed on the basis of the X-ray structural properties which show that the two lanthanide sites are structurally different. MCD spectroscopy of the dysprosium(III) and neodymium(III) complexes ($[Dy^{III}_2(L)(OAc)_4]^+$ and $[Nd^{III}_2(L)(OAc)_4]^+$) allowed us to thoroughly analyze the ligand field, and high-frequency EPR spectroscopy of the gadolinium(III) species ($[Gd^{III}_2(L)(OAc)_4]^+$) showed the importance of dipolar coupling in these systems. An extensive quantum-chemical analysis of the dysprosium(III) complex ($[Dy^{III}_2(L)(OAc)_4]^+$), involving an ab initio (CASSCF) wave function, explicit spin−orbit coupling (RASSI-SO), and a ligand field analysis (Lines model and Stevens operators), is in full agreement with all experimental data (SQUID, HF-EPR, MCD) and specifically allowed us to accurately simulate the experimental χT versus T data, which therefore allowed us to establish a qualitative model for all relaxation pathways.

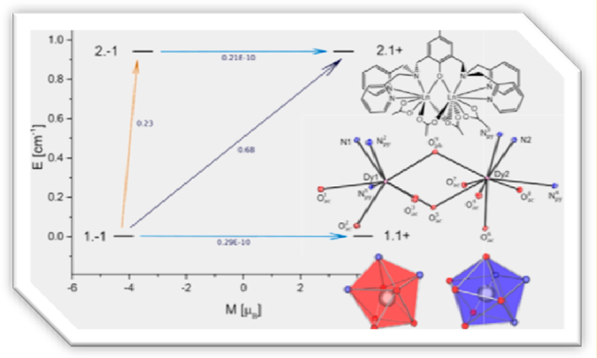

■ INTRODUCTION

Single molecular magnetism (SMM) was first described some 25 years ago and has since attracted much attention,[1−4] not only due to a number of possible applications[5,6] but also because the fundamental reasons for bistability and relaxation, specifically the anisotropy barrier and quantum tunneling, are known to be related to the electronic structure of the metal sites, magnetic exchange, and magnetic anisotropy.[7−9] These are related to molecular structure, and therefore in theory are predictable.[10] While the investigation of SMMs in the 1990s focused on oligonuclear 3d metal complexes,[11] the larger spin−orbit coupling of second and third row transition metal ions and the lanthanides, specifically the large intrinsic anisotropy of the lanthanides, more recently started to attract attention and resulted in an increasing number of oligonuclear lanthanide and mixed-metal complexes with SMM behavior.[12−16] Major problems in this area still are the predictability of structures and their correlation with electronic properties,[12,17] but interesting developments in theory may help to more deeply understand experimental data on coupled lanthanide systems and eventually lead to a basis which may enable us to optimize lanthanide-based molecular magnets.[18−22]

We report a series of eight isostructural homodinuclear lanthanide(III) complexes with the general formula $[Ln_2L(OAc)_4]PF_6$, where Ln^{III} = Y, Nd, Gd, Tb, Dy, Ho, Er, and Lu and L = 2,6-bis((bis(pyridin-2-ylmethyl)amino)methyl)-4-methylphenolate (see Chart 1). The aim was to thoroughly investigate the magnetic exchange between the lanthanide centers, in particular to fully understand the electronic structure

Chart 1. Structure of the Ligand L

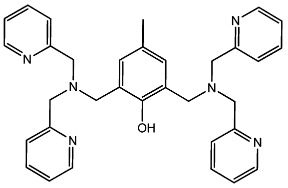

Received: July 30, 2015
Published: November 20, 2015

DOI: 10.1021/acs.inorgchem.5b01673
Inorg. Chem. 2015, 54, 11247−11258

and to quantify the anisotropy. We have used experimental structural, magnetic, optical spectroscopic, and high-field electron paramagnetic resonance data and have also analyzed the system computationally with ab initio CASSCF calculations and introduced spin−orbit coupling via the restricted active space state interaction method (RASSI).[23] The magnetic coupling was then analyzed on the basis of the "Lines model",[24] combined with a thorough ligand field analysis, based on extended Stevens operators,[25] using the quantum-chemical data. This allowed us to fully interpret the experimental data and, importantly, to carefully check for consistency between the various experimental and computational data sets. Therefore, the combined experimental and computational analysis serves as a benchmark for the theoretical model, which may now be used for the design and optimization of lanthanide-based SMMs.

■ RESULTS AND DISCUSSION

Syntheses and Structural Properties. The preparation of the homodinuclear lanthanide complexes involved lanthanide(III) acetate salts and the dinucleating ligand L (Chart 1). The complexes of Y^{III}, Nd^{III}, Gd^{III}, Tb^{III}, Dy^{III}, Ho^{III}, Er^{III}, and Lu^{III} were isolated and characterized;, from all but Nd^{III} X-ray crystal structures were obtained. All structures are isomorphous and contain approximately three molecules of methanol per complex in the crystal lattice.

Figure 1 shows the molecular structure of the bis-dysprosium(III) complex, and similar structural plots of all other complexes are given as Supporting Information; selected structural parameters of all structures are listed in Table 1. The cations are asymmetric with different coordination numbers at the two lanthanide centers (Ln1 is 8-coordinate with an N_3O_5 chromophore, Ln2 is 9-coordinate with an N_3O_6 donor set). L provides two pyridine and a tertiary amine donor to each site; the two metal cations are bridged by the μ_2-OPh phenolate of the dinucleating ligand and by two acetate anions. The latter have different bonding modes: one is terminal at the 9-coordinate center 2 and bridges to the other center via a μ_1-O^5_{Ac} oxygen atom. The other acetate at site 2 is a μ_2-CH_3COO-$\kappa^2O{:}O'$ moiety and coordinates to the two centers with a μ_1-O^3_{Ac} and an O^4_{Ac} atom. Both metal centers are also coordinated to terminal acetates. The average Ln^{III}−O distances vary significantly, and the distance between the two metal ions is between 3.767 Å (Er^{III}) and 3.812 Å (Tb^{III}, see Table 1). The inner coordination sphere of the 9-coordinate site 2 is best described as a monocapped distorted antiprism, and the 8-coordinate site 1 is a triangular dodecahedron; both centers have highly distorted icosahedral symmetry (see Figure 1).

Intermolecular magnetic exchange often plays an important role in magnetic and spectroscopic properties of solids.[26] Therefore, as an example the structure of the dinuclear Dy^{III}_2 complex was evaluated for intermolecular interactions. It appears that there is only one significant intermolecular contact, i.e., a π−π interaction (see Figure 2): the bridging phenolate ring (Ph) aligns with a pyridine donor of the 8-coordinated site 1 (py1) as well as a pyridine moiety of the 9-coordinated site 2 (py2). The distances and angles between the aromatic rings are also summarized in Table 1.

Electronic Properties. *i. Magnetism.* Direct current (dc) magnetic susceptibilities were measured on powdered crystals of the samples used for crystallography at 500 G over a temperature range 2−300 K. $\chi_M T$ versus T plots of all $[Ln_2(L)(OAc)_4]PF_6$ complexes are shown in Figure 3.

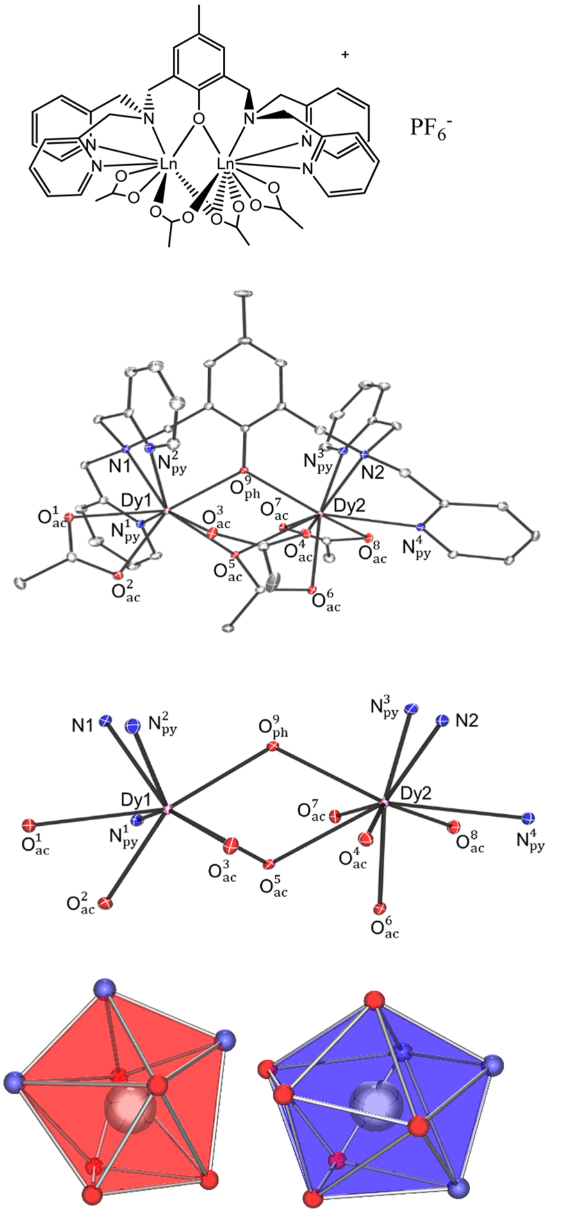

Figure 1. Chemical structure, ORTEP plot of the full structure (hydrogen atoms and anions omitted) and of the inner coordination sphere of $[Dy^{III}_2(L)(OAc)_4]^+$, and coordination polyhedra of the two lanthanide sites (left, blue, 8-coordinate Dy1 site; right, red, 9-coordinated Dy2 site).

The $\chi_M T$ value of the dinuclear Nd^{III}_2 species at 300 K is 2.94 cm^3 K mol^{-1}; for two independent Nd^{III} ions with a $^4I_{9/2}$ ground state a somewhat higher $\chi_M T$ value of 3.28 cm^3 K mol^{-1} is expected at ambient temperature. In a known alkoxy-bridged dinuclear Nd^{III} complex, a similar value for $\chi_M T$ = 2.84 cm^3 K mol^{-1} was observed at 300 K.[27] The $\chi_M T$ value decreases steadily with decreasing temperature to a value of 0.94 cm^3 K mol^{-1} at 2.3 K, in agreement with antiferromagnetic intramolecular coupling.

The $\chi_M T$ value of the Gd^{III}_2 complex is 15.10 cm^3 K mol^{-1} at 300 K, somewhat smaller than the expected value 15.82 cm^3 K mol^{-1} of two uncoupled $^8S_{7/2}$ centers. $\chi_M T$ slowly decreases to 14.16 cm^3 K mol^{-1} at 23.3 K and drops to 9.71 cm^3 K mol^{-1} at 2.0 K. The almost temperature independent shape for a dinuclear Gd^{III} species[28] indicates a weak antiferromagnetic

Table 1. Selected Inter- and Intramolecular Distances (Å) and Angles (deg) of $[\mathrm{Ln^{III}}_2(\mathrm{L})(\mathrm{OAc})_4]\mathrm{PF_6}\cdot n\mathrm{MeOH}$

	$[\mathrm{Ln^{III}}_2(\mathrm{L})(\mathrm{OAc})_4]^+$						
	Y	Gd	Tb	Dy	Ho	Er	Lu
Ln1−Ln2	3.775(3)	3.791(1)	3.812(2)	3.794(1)	3.773(2)	3.767(1)	3.729(1)
Ln1−$\mathrm{O}^{1}_{\mathrm{AC1}}$	2.363(4)	2.373(2)	2.381(3)	2.372(2)	2.360(3)	2.353(2)	2.324(2)
Ln1−$\mathrm{O}^{2}_{\mathrm{AC}}$	2.373(4)	2.407(2)	2.400(3)	2.385(2)	2.372(3)	2.372(2)	2.353(2)
Ln1−$\mathrm{O}^{3}_{\mathrm{AC}}$	2.284(4)	2.313(2)	2.305(3)	2.299(2)	2.283(3)	2.271(2)	2.241(2)
Ln1−$\mathrm{O}^{5}_{\mathrm{AC}}$	2.276(4)	2.317(1)	2.307(3)	2.304(2)	2.285(3)	2.277(1)	2.251(2)
Ln2−$\mathrm{O}^{4}_{\mathrm{AC}}$	2.347(4)	2.375(2)	2.373(3)	2.354(2)	2.345(3)	2.340(2)	2.310(2)
Ln2−$\mathrm{O}^{5}_{\mathrm{AC}}$	2.450(4)	2.464(2)	2.473(3)	2.459(2)	2.445(3)	2.439(2)	2.419(2)
Ln2−$\mathrm{O}^{6}_{\mathrm{AC}}$	2.456(4)	2.508(2)	2.493(3)	2.477(2)	2.459(3)	2.446(2)	2.415(3)
Ln2−$\mathrm{O}^{7}_{\mathrm{AC}}$	2.402(4)	2.438(2)	2.425(3)	2.415(2)	2.399(3)	2.392(2)	2.372(2)
Ln2−$\mathrm{O}^{8}_{\mathrm{AC}}$	2.408(4)	2.432(2)	2.420(3)	2.410(2)	2.401(3)	2.402(2)	2.385(2)
Ln1−$\mathrm{O}^{9}_{\mathrm{Ph}}$	2.312(4)	2.334(1)	2.340(3)	2.313(2)	2.314(3)	2.308(2)	2.273(2)
Ln2−$\mathrm{O}^{9}_{\mathrm{Ph}}$	2.342(4)	2.360(1)	2.358(3)	2.356(2)	2.339(3)	2.330(1)	2.300(2)
Ln1−N1	2.549(4)	2.570(2)	2.572(3)	2.563(2)	2.549(3)	2.540(2)	2.513(2)
Ln2−N2	2.585(5)	2.633(2)	2.603(4)	2.594(2)	2.579(4)	2.580(2)	2.553(3)
Ln1−$\mathrm{N}^{1}_{\mathrm{Py}}$	2.536(5)	2.575(2)	2.557(4)	2.548(2)	2.535(4)	2.523(2)	2.499(3)
Ln1−$\mathrm{N}^{2}_{\mathrm{Py}}$	2.535(5)	2.570(2)	2.548(4)	2.536(2)	2.517(4)	2.518(2)	2.498(3)
Ln2−$\mathrm{N}^{3}_{\mathrm{Py}}$	2.552(5)	2.557(2)	2.562(3)	2.552(2)	2.538(3)	2.532(2)	2.508(3)
Ln2−$\mathrm{N}^{4}_{\mathrm{Py}}$	2.554(4)	2.558(2)	2.578(3)	2.562(2)	2.557(3)	2.550(2)	2.525(2)
∠Ln1−$\mathrm{O}^{9}_{\mathrm{Ph}}$−Ln2	108.44(15)	107.73(6)	108.50(11)	108.73(6)	108.35(11)	108.61(6)	109.25(8)
Py2′−Py1	4.073	4.040	4.085	4.084	4.081	4.135	4.090
Py1−Ph	3.843	3.857	3.867	3.858	3.837	3.847	3.813
Ph−Py2	3.471	3.453	3.477	3.473	3.464	3.462	3.458
Py2−Py1′	4.073	4.040	4.085	4.084	4.081	4.135	4.090
∠Py2′−Py1	21.86	20.45	20.80	21.68	22.03	23.04	23.37
∠Py1−Ph	37.87	38.40	38.36	38.24	38.28	38.62	37.86
∠Ph−Py2	20.64	20.93	20.46	20.77	20.53	20.24	20.29
∠Py2−Py1′	21.86	20.45	20.80	21.68	22.03	23.04	23.37

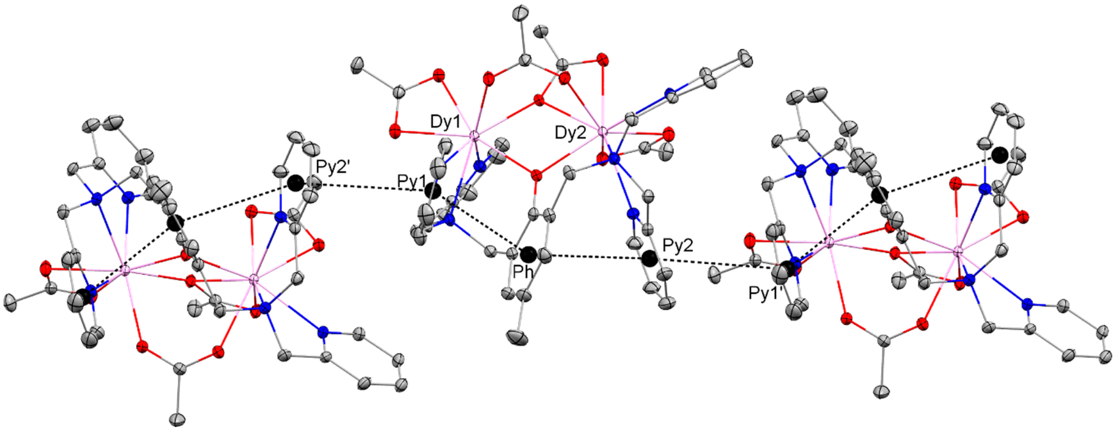

Figure 2. Mercury plot for the $[\mathrm{Dy^{III}}_2(\mathrm{L})(\mathrm{OAc})_4]^+$ and its neighboring molecules. Black spheres show ring centroid for the interacting pyridines and phenols. The dashed lines show the direct contact to the next aromatic ring.

interaction between the $\mathrm{Gd^{III}}$ centers. With the known isotropic interaction, the Hamiltonian $\hat{H} = -J\hat{S}_{\mathrm{Gd1}}\hat{S}_{\mathrm{Gd2}}$ results in the formula for the temperature dependence of the molar magnetic susceptibility in eq 1[29]

$$\chi_{\mathrm{M}} = \frac{2g^2N\beta^2}{kT} \times [140\mathrm{e}^{56J/kT} + 91\mathrm{e}^{42J/kT} + 55\mathrm{e}^{30J/kT} + 30\mathrm{e}^{20J/kT} + 14\mathrm{e}^{12J/kT} + 5\mathrm{e}^{6J/kT} + \mathrm{e}^{2J/kT}]/[15\mathrm{e}^{56J/kT} + 13\mathrm{e}^{42J/kT} + 11\mathrm{e}^{30J/kT} + 9\mathrm{e}^{20J/kT} + 7\mathrm{e}^{12J/kT} + 5\mathrm{e}^{6J/kT} + 3\mathrm{e}^{2J/kT} + 1] \quad (1)$$

where g is the Landé factor, β the Bohr magneton, N the Avogadro number, and k the Boltzmann constant; a good fit of the experimental data is found with $J = -0.065$ cm^{-1} and $g = 1.97$. The small coupling strength J obtained from the fit is indeed in agreement with the hypothesis from the thermal evolution of the $\chi_{\mathrm{M}}T$ curve. Other comparable dinuclear $\mathrm{Gd^{III}}$ complexes have only slightly larger antiferromagnetic coupling constants.[30]

The $\chi_{\mathrm{M}}T$ value of the $\mathrm{Tb^{III}}_2$ compound at 300 K with 24.10 cm^3 K mol^{-1} is higher than the expected value of 22.78 cm^3 K mol^{-1} for a $^7F_6$ ground state. With a decrease in the temperature to 60 K, there is a small decrease to 22.86 cm^3 K mol^{-1}, with 16.42 cm^3 K mol^{-1} at 2 K.

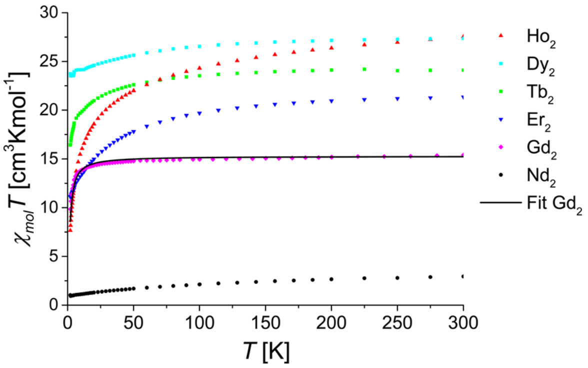

Figure 3. $\chi_M T$ vs T plot of all $[\mathrm{Ln^{III}}_2(\mathrm{L})(\mathrm{OAc})_4]\mathrm{PF}_6$ complexes together with a fit of the $\mathrm{Gd^{III}}$ compound (eq 1, g = 1.97, J = −0.065 $\mathrm{cm^{-1}}$).

The $\chi_M T$ value of 27.34 $\mathrm{cm^3\ K\ mol^{-1}}$ for the $\mathrm{Dy^{III}}_2$ complex at 300 K is lower than the expected value of 28.36 $\mathrm{cm^3\ K\ mol^{-1}}$ for a $^6H_{15/2}$ ground state. This decreases slightly down to a minimum of 23.52 $\mathrm{cm^3\ K\ mol^{-1}}$ at 2.3 K and then slightly rises to 23.73 $\mathrm{cm^3\ K\ mol^{-1}}$ at 2 K.

The $\chi_M T$ value for the $\mathrm{Ho^{III}}_2$ species at 300 K is 27.54 $\mathrm{cm^3\ K\ mol^{-1}}$, i.e., lower than the theoretical value of 28.10 $\mathrm{cm^3\ K\ mol^{-1}}$ for a $^5I_8$ ground state. With a continuous decrease it reaches 7.66 $\mathrm{cm^3\ K\ mol^{-1}}$ at 2 K.

The $\chi_M T$ value of the dinuclear $\mathrm{Er^{III}}_2$ complex is 21.36 $\mathrm{cm^3\ K\ mol^{-1}}$ at 300 K, significantly lower than the expected 22.95 $\mathrm{cm^3\ K\ mol^{-1}}$ for two uncoupled centers with a $^4I_{15/2}$ ground state. After a continuous decrease, $\chi_M T$ reaches 11.11 $\mathrm{cm^3\ K\ mol^{-1}}$ at 2 K.

As described above, the general feature of the $\chi_M T$ curves for the four heavy lanthanide complexes is very similar. The continuous decrease of $\chi_M T$ with the decrease of temperature could partially result from thermal depopulation of the Stark levels, i.e., from the splitting of the free-ion ground state of $\mathrm{Ln^{III}}$ by the crystal field. On the basis of the analysis of the data of the $\mathrm{Gd^{III}}$ compound, the exchange coupling between the lanthanides in these four isostructural dinuclear compounds is probably also antiferromagnetic in nature, but should be very weak to the point of being virtually nonexistent.

For the $\mathrm{Dy^{III}}_2$ complex the temperature dependent ac susceptibility data were also collected (see Supporting Information). The isolines are split in the out-of-phase susceptibility. No maximum is observed, implying that this may occur below 1.8 K, the lowest possible temperature of the setup used. This indicates only very weak SMM behavior. Very rough estimates of U_{eff} and τ_0 may be obtained from eq 2[31,17]

$$\ln(\chi''/\chi') = \ln(\omega\tau_0) + U_{\mathrm{eff}}/kT \tag{2}$$

leading to $U_{\mathrm{eff}} \sim 1.97$ K and $\tau_0 = 1.62 \times 10^{-6}$ s. This is comparable to barriers of similar compounds.[31]

ii. High-Frequency EPR Spectroscopy. Representative HF-EPR spectra of the $\mathrm{Gd^{III}}_2$ complex obtained at 4 K display broad resonance features (see Figure 4). The shape of a particular resonance feature allows qualitative conclusions about the presence and the sign of anisotropy as maximum absorption appears in the lower field region of the resonances while the resonance intensity smoothly decreases as the magnetic field increases. Such a behavior in general suggests an easy-axis-type of anisotropy. To be specific, maximum absorption at low field and at low temperature indicates the ground state transition for the magnetic field parallel to the easy axis.[32,33] We note that this behavior does not appear in randomly oriented powder spectra, but it is typical for the particular case of the aligned powder, i.e., where all local anisotropy axes are aligned along the applied magnetic field. As will be described below, our analysis suggests a dipolar origin of the anisotropy. The temperature dependence of the spectra at 130 GHz supports the easy axis scenario as spectral weight is shifted from lower to higher magnetic field upon heating (see Supporting Information). The anisotropy is, however, small so that the excited state transitions and the low-lying state transitions are not clearly separated. We attribute the broad shoulder seen in the resonance features to only partially separated resonances.

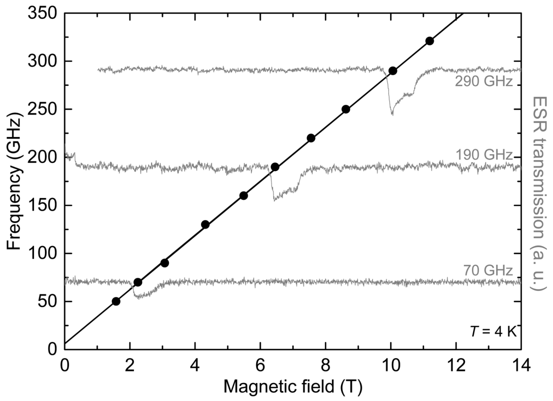

Figure 4. Resonance frequencies vs magnetic field of the dinuclear $\mathrm{Gd^{III}}$ complex, at 4 K (●). Representative EPR spectra are shown as gray lines. The black solid line displays the simulated frequency dependence of the ground state resonance for magnetic fields parallel to the easy axis. Parameters are given in the text. Note that the linear fit to the data mentioned in the text nearly perfectly coincides with the simulated data and hence is not shown.

The resonance fields of the ground state transition at 4 K are shown in the resonance frequency versus magnetic field diagram in Figure 4. Linear fitting of the resonance branches provides the g-factor and the zero-field splitting (ZFS), i.e., g = 2.01 ± 0.01 and Δ = 5.9 ± 1.0 GHz. We mention the nonvanishing size of the ZFS which in the case of $\mathrm{Gd^{III}}$ ions with a half-filled 4f-shell and negligible spin−orbit coupling does not originate from single-ion anisotropy. We conclude that magnetic dipolar coupling accounts for the observed ZFS.

Quantitatively, the magnetic anisotropy tensor induced by magnetic dipolar coupling for weakly coupled pairs of ions is written as in eq 3.[34−36] In eq 3, $\beta_r = \mu_B{}^2/r^3$; μ_B is the Bohr

$$\vec{D}_{dipolar} = \begin{pmatrix} g_x{}^2(1-3\sin^2\eta\sin^2\xi) & -3g_xg_y\sin^2\xi\sin\eta\cos\eta & -3g_xg_z\sin\xi\cos\xi\sin\eta \\ -3g_yg_x\sin^2\xi\sin\eta\cos\eta & g_y{}^2(1-3\cos^2\eta\sin^2\xi) & -3g_yg_z\sin\xi\cos\xi\cos\eta \\ -3g_zg_x\sin\xi\cos\xi\sin\eta & -3g_zg_y\sin\xi\cos\xi\cos\eta & g_z{}^2(1-3\cos^2\xi) \end{pmatrix}\beta_r \tag{3}$$

magneton, and r is the distance between two ions (r = 3.791 Å for the $\mathrm{Gd^{III}}$ dinuclear complex at hand). $\xi(\eta)$ is the angle between the ionic z (y)-axis and the distance vector $\hat{r}$. All the terms here are referred from ref 35. The spin Hamiltonian including the anisotropy term induced by magnetic dipolar coupling can be written as in eq 4

$$\hat{H} = -J\hat{S}_1\cdot\hat{S}_2 + g\mu_B\sum_{i=1}^{2}\hat{S}_i\cdot\hat{B} + \hat{S}_1\cdot\vec{D}_{\mathrm{dipolar}}\cdot\hat{S}_2 \tag{4}$$

with the intradimer exchange integral J extracted from the magnetic susceptibility. The Hamiltonian of eq 4 is applied to

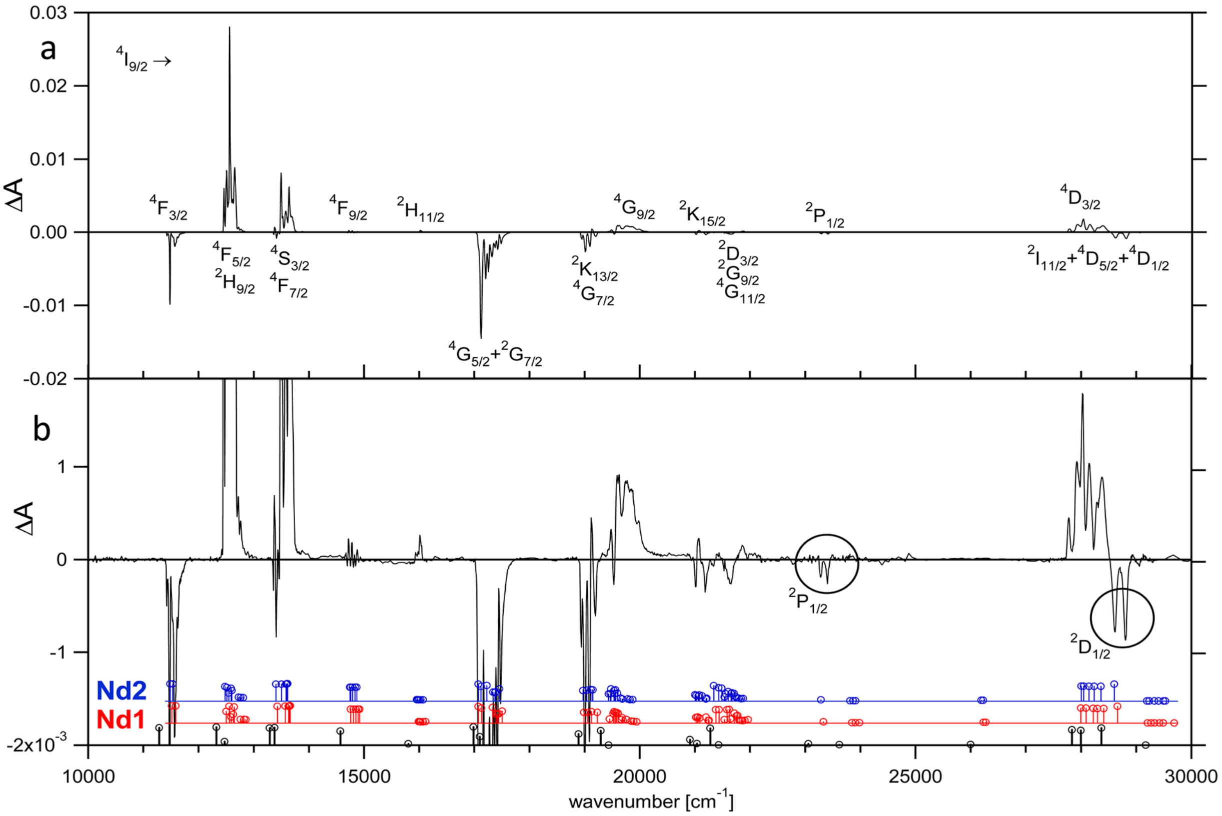

Figure 5. (a) Overview of the $[\mathrm{Nd}^{\mathrm{III}}{}_2(\mathrm{L})(\mathrm{OAc})_4]^+$ MCD spectrum at 8.0 K and 5.0 T. (b) As above, scaled to show the weaker transitions. The stick spectra are the calculated values for the free ion (black), the Nd1 center (red), and the Nd2 center (blue). The transitions to the $^2P_{1/2}$ and $^2D_{1/2}$ states are seen for both centers as indicated. The observed and calculated peak positions are given as Supporting Information.

simulate the ZFS for the magnetic field parallel to the easy axis. η does not affect the results significantly for the magnetic field parallel to the easy axis. The best simulation parameters with $\xi = 30°$, $\eta = 0°$, and isotropic $g = 2.01$ for a Gd^{3+} ion yields $\Delta = 6.00$ GHz, which matches the experimental results of $\Delta = 5.9 \pm 1.0$ GHz. Our analysis hence confirms the dipolar origin of ZFS observed in the HF-EPR data of the $\mathrm{Gd}^{\mathrm{III}}$ dinuclear complex. We note that when the magnetic field determines the easy axis direction, the observed easy-axis-like behavior for the aligned case is straightforwardly explained.

iii. MCD Spectroscopy. Figures 5a and 6a show an overview of the MCD spectra of the $[\mathrm{Nd}_2(\mathrm{L})(\mathrm{OAc})_4]^+$ and $[\mathrm{Dy}_2(\mathrm{L})(\mathrm{OAc})_4]^+$ complexes, respectively, together with the assignment of the bands to transitions between appropriate multiplets; detailed spectra of particular transitions are shown in Figures 7 and 8, respectively. The spectra were obtained from the complexes dissolved in a 3:1 ethanol/methanol glass at 5 T and 8 K. The absorption electronic spectra were measured simultaneously, but were generally of low quality due to the low extinction coefficients and a background that was difficult to subtract. The phase-sensitive detection employed in the MCD measurement is more sensitive to small signals, has minimal background, and allows the f−f transitions to be clearly observed.

The spectra can be interpreted in terms of a superposition of the single ion spectra of f−f transitions. For Nd (Dy) there are a total of 182 (1001) Kramers doublets, of which there are 96 (116) expected to occur in the 9000−30 000 cm^{-1} spectral range. As each lanthanide site in the $[\mathrm{Ln}_2(\mathrm{L})(\mathrm{OAc})_4]^+$ complexes experiences a different ligand field, their superimposed spectra give rise to a large number of transitions, and the discussion of the spectra is guided by ligand field calculations.

Ligand Field Calculations. The calculations of the ligand-field-split states of the dinuclear complexes are made assuming that the interaction between the centers is weak, i.e., that the optical spectra can be interpreted in terms of a superposition of single ion spectra. The Hamiltonian to be solved is the usual series of atomic terms together with the ligand field of the atomic environment. The atomic terms include the electron−electron repulsion (F^2, F^4, F^6), spin−orbit coupling (ζ), and the higher order terms that include the two body configuration interaction parameters (α, β, γ), the three body parameters (T^k, $k = 2, 3, 4, 6, 7, 8$), the magnetic parameters (M^k, $k = 0, 2, 4$), describing the spin−spin and spin−other orbit interactions, and the electrostatically correlated spin−orbit interaction (P^k, $k = 2, 4, 6$). These 19 atomic parameters for $\mathrm{Nd}^{\mathrm{III}}$[37] and $\mathrm{Dy}^{\mathrm{III}}$[38]were taken from the literature, where they were obtained from the fitting to LnCl_3 spectra. These data sets are considered reliable and not plagued by errors due to the use of incorrect reduced matrix elements as in other calculations. Details of the ligand field calculations are tabulated in the Supporting Information.

For a lanthanide ion in a ligand field with no formal symmetry, there are 27 nonzero B_{kq} parameters,[39] far more than can reasonably be determined with the available experimental data. Here, we make use of the relationship between the angular overlap model (AOM) and the B_{kq} parameters.[39] In this manner, the ligand field is determined by the geometry of the first coordination sphere and adjustable e_σ, e_π parameters. Details of the ligand field parametrization are given in the Supporting Information. The calculation of the f state energy levels is well-known.[39−41] Good agreement was found with

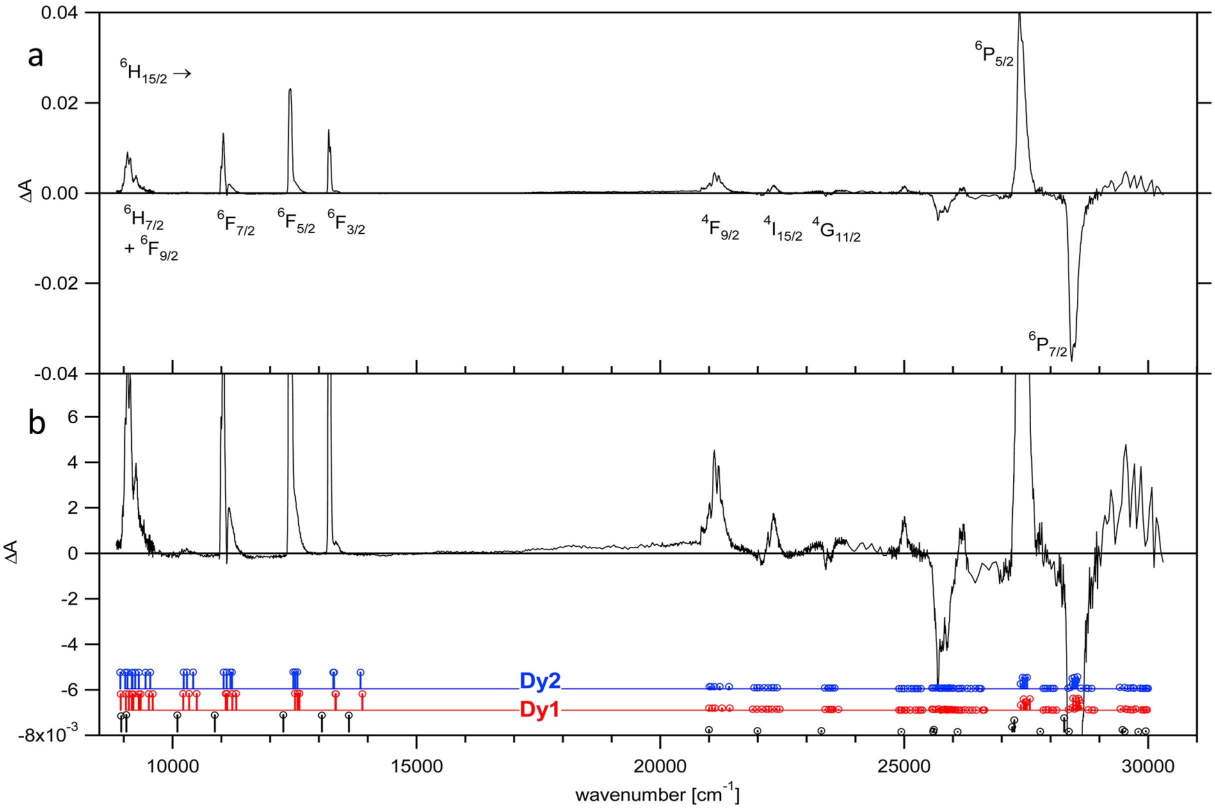

Figure 6. (a) Overview of the $[Dy^{III}_2(L)(OAc)_4]^+$ MCD spectrum at 8.0 K and 5.0 T. (b) As above, scaled to show the weaker transitions. The stick spectra are the calculated values for the free ion (black), the Nd1 center (red), and the Nd2 center (blue). The observed and calculated peak positions are given as Supporting Information.

calculations, where the spin−spin interaction part of M^k parameters was included.[37] As we are interested in the interaction of the energy levels with a magnetic field we have also calculated the *g*-values, assuming isolated Kramers doublets. We have used an established methodology[42] to calculate and diagonalize the g^2-tensor, which gives the principle values and directions (see Supporting Information).

Discussion of the Spectra. Figures 5b and 6b show a more detailed view of the spectra, and these also include stick spectra of the calculated energy positions of the free ion (black) as well as for each lanthanide center Ln1 (red) and Ln2 (blue). The height of the stick spectra is the fraction of the calculated wave function that has the same spin as the ground state, which gives some indication of the relative intensity of the transitions. The experimental and calculated energies for each lanthanide center are given as Supporting Information. It is important to note that no fitting of the parameters to the experimental spectra has been attempted, as the spectra of the superimposed centers need 73 (19 + 2 × 27) parameters. However, some insights can be gained from using the same atomic parameters for each center, with different ligand fields specific to Ln1 and Ln2 being used. Therefore, for $[Nd^{III}_2(L)(OAc)_4]^+$ and $[Dy^{III}_2(L)(OAc)_4]^+$ the same ligand fields are used for the Ln1 and Ln2 coordination geometry.

Comparing the calculated stick spectra for Nd1 and Nd2 in Figure 5b, one can see the shift of the free-ion levels (black) to higher energy (red/blue) when the ligand field is added to give good agreement with the experimental levels. The spread of the calculated levels and that of the experiment also agree quite well. In general, the experimental intensities correlate with the calculated fractional spin composition.

Figure 7 displays the temperature dependence of the $[Nd^{III}_2(L)(OAc)_4]^+$ spectra in the region of the $^4I_{9/2} \rightarrow {}^4G_{5/2}$ and $^4I_{9/2} \rightarrow {}^4D_{5/2}, {}^4D_{3/2}, {}^4D_{1/2}$ transitions, clearly showing the C-term behavior expected for this odd electron system. With a fit of the integrated intensity to a simple $S = {}^1/_2$ function in a VTVH plot, one finds effective *g*-values of 4.850 and 3.197 from the temperature dependence of the $^4I_{9/2} \rightarrow {}^4G_{5/2}$ and $^4I_{9/2} \rightarrow {}^4D_{5/2}, {}^4D_{3/2}, {}^4D_{1/2}$ groups of transitions, respectively. In a comparison of the calculated ground state *g*-values of Nd1 (0.405, 0.977, 4.958) and Nd2 (0.006, 1.618, 3.561, see Supporting Information), this suggests that the former transition is *xy* polarized while the latter may have *xy* and *z* polarized components. The negative MCD signals of the $^4I_{9/2} \rightarrow {}^4D_{1/2}$ transitions in Figure 7 are interesting, as there is only a single predicted transition. The ∼190 cm^{-1} separation of these peaks must therefore be due to the $^4I_{9/2} \rightarrow {}^4D_{1/2}$ transitions of each metal site. The $^4D_{1/2}$ state in Nd1 is calculated to be 60 cm^{-1} higher than that in Nd2. A calculation of the energy levels as a function of the ligand field strength is shown in the Supporting Information, and the $^4D_{1/2}$ state remains separate from the nearby bands. Another calculated isolated single state is $^2P_{1/2}$ at ∼23 300 cm^{-1} (Supporting Information), and indeed, two peaks are observed in this region (see Figure 5b and Supporting Information). Again, the higher energy peak is predicted to be due to Nd1, but the calculated separation of 15 cm^{-1} is significantly smaller than that observed (123 cm^{-1}), indicating that the difference in the ligand fields between the two sites may be larger than assumed here.

The $[Dy_2(L)(OAc)_4]^+$ spectrum shown in Figure 6a is dominated by the $^6H_{15/2} \rightarrow {}^6F_n$ ($n = {}^9/_2, {}^7/_2, {}^5/_2, {}^3/_2$) transitions in the near-infrared and the $^6H_{15/2} \rightarrow {}^6P_{5/2}, {}^6P_{7/2}$

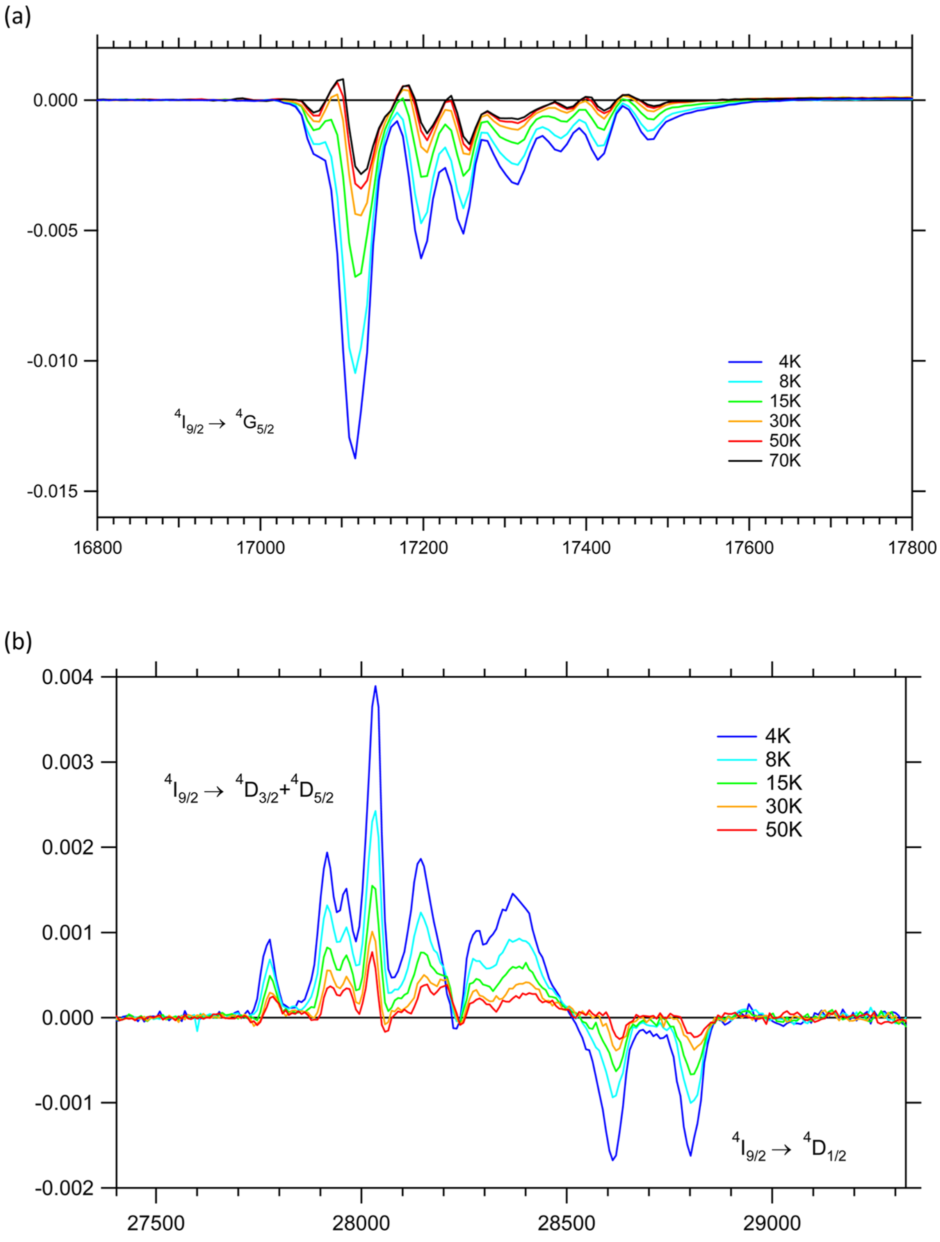

Figure 7. (a) MCD spectrum of $[Nd^{III}_2(L)(OAc)_4]^+$, showing the transitions of the $^4I_{9/2} \rightarrow {}^4G_{5/2}$ multiplet as a function of temperature. (b) MCD spectrum of $[Nd^{III}_2(L)(OAc)_4]^+$, showing the transitions of the $^4I_{9/2} \rightarrow {}^4D_{5/2} + {}^4D_{3/2}$ multiplets as a function of temperature.

transitions in the blue region. At energies above 20 000 cm^{-1}, the quartet and sextet states are very mixed (see Supporting Information) although it is easy to identify the 3 components of the $^6P_{5/2}$ and the 4 components of the $^6P_{7/2}$ states embedded in the quartet states. The transitions to the components of these two states appear as a single positive band and a single negative band, respectively.

The $^6H_{15/2} \rightarrow {}^6F_{1/2}$ transition is calculated to be an isolated single peak, but as shown in Figure 8a, it does not appear experimentally. This is due to the $\Delta J > 6$, involved for this transition which results in it being forbidden.[43] However, the small splitting observed in the $^6H_{15/2} \rightarrow {}^6F_{3/2}$ transition is likely due to the two lanthanide sites as the calculated separation of the two $^6F_{3/2}$ components within each Dy site is 8 (Dy1) and 2 (Dy2) cm^{-1}, while the separation of the mean energies between the two sites is 40 cm^{-1}, which is reasonably close to the observed 35 cm^{-1}. The observed 23 cm^{-1} splitting in the $^6H_{15/2} \rightarrow {}^6F_{5/2}$ transition is more ambiguous, as the splitting between the $^6F_{5/2}$ components is comparable with energy differences between the two sites.

Figure 8b shows the temperature dependence of the $^6H_{15/2} \rightarrow {}^6F_{7/2}$ transition. This is less than that observed in the $[Nd^{III}_2(L)(OAc)_4]^+$ complex, implying a larger *g*-value. At the lower edge of the band, derivative shaped A-terms develop, implying a difference in the ground and excited state *g*-values, so that transitions of the opposite sign form an A-term rather than cancel as seen in the $[Nd^{III}_2(L)(OAc)_4]^+$ spectra of Figure 7. The additional A-term that appears at higher temperatures 81 cm^{-1} to lower energy is then a hot band due to the population of higher levels of the split ground state. The calculated first energy levels of 39 (Dy1) and 44 (Dy2) cm^{-1} again may indicate that the ligand field is larger than estimated.

Computation of the Electronic Properties. The calculation of the wave function was done with ab initio

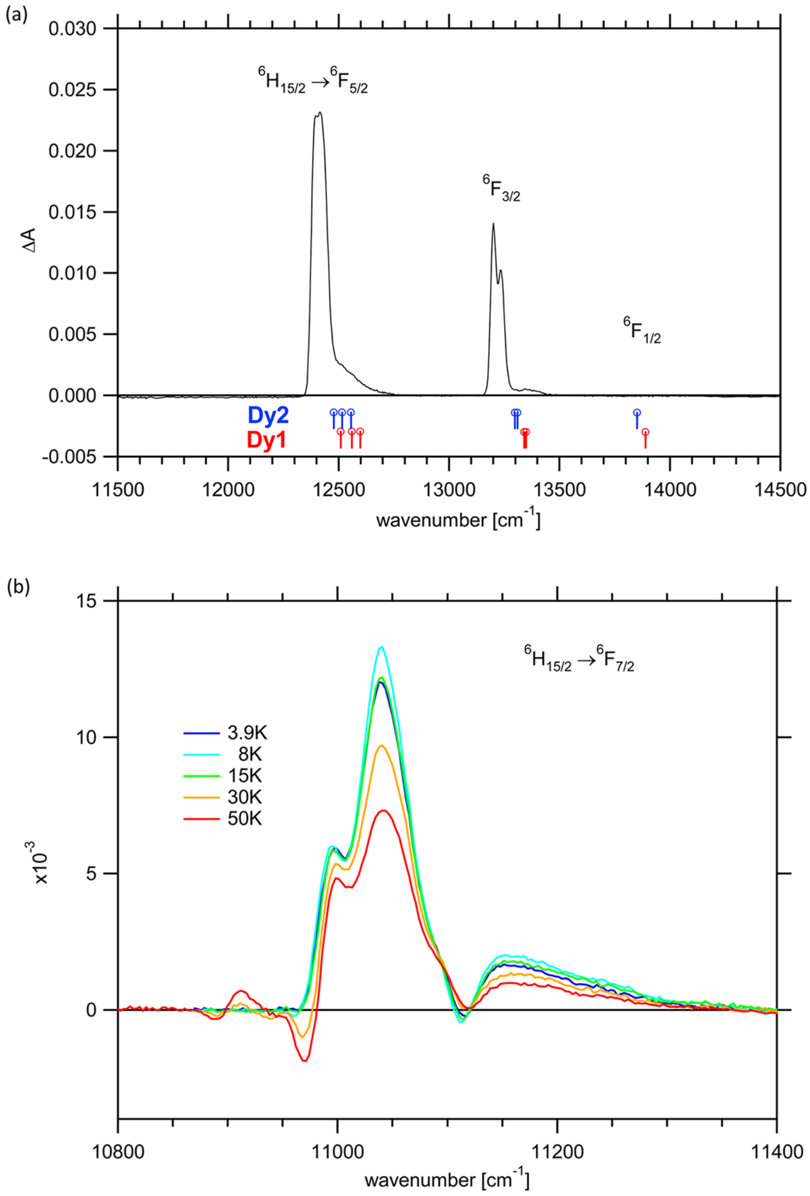

Figure 8. (a) MCD spectrum of $[Dy^{III}_2(L)(OAc)_4]^+$, showing the transitions of the $^6H_{15/2} \rightarrow {}^6F_{5/2}$, $^6F_{3/2}$ multiplets. Note the complete absence of the $^6H_{15/2} \rightarrow {}^6F_{1/2}$ transition. The calculated positions of the Dy1 (red) and Dy2 (blue) centers are shown as stick spectra. (b) MCD spectrum of $[Dy^{III}_2(L)(OAc)_4]^+$, showing the transitions of the $^6H_{15/2} \rightarrow {}^6F_{7/2}$ multiplet as a function of temperature.

calculations on the crystal structural coordinates with Molcas 8.0.[44] An established fragmentalized approach was used, where the neighboring magnetic centers are substituted with their closest diamagnetic analogue; i.e., Dy^{III} was substituted by Lu^{III} with an ionic radius closer than that of La^{III}.[19] This results in two fragments with only one magnetic center to calculate. All atoms were described by contracted ANO-RCC basis sets, included in Molcas.[45] The active space of the employed CASSCF method included nine electrons in seven 4f orbitals. Additional dynamic correlation through second-order perturbation theory was not considered, since the effect is known to be small for lanthanides.[46] From the ligand field manifold for a $4f^9$ electronic configuration arise 21 sextet, 224 quartet, and 490 doublet states. Sufficient results can be obtained with all sextet, 50 doublet, and 50 quartet states. Considering more roots increases calculation time and demand drastically and has very little influence on the energy of the ground and low-lying excited states, since they correspond to high-energy states that only have a small contribution. After obtaining the spin-free wave functions through CASSCF,[47] spin−orbit coupling was introduced via the restricted active space state interaction method (RASSI).[23] Due to the high number of states arising from the given active space, only a limited number can be mixed by spin−orbit coupling. All sextet, 50 doublet, and 50 quartet states were considered. The resulting RASSI-SO-coupled multiplet states were introduced to the Molcas SINGLE-ANISO module[44] to calculate the local electronic and magnetic properties of the single magnetic center fragments.

To further account for the magnetic coupling between the two lanthanide centers the "Lines model" was applied.[24] Even though this is a solid state isotropic exchange model, one can apply the effective Hamiltonian on the anisotropic basis (spin−orbit coupled multiplets from RASSI), calculated for the single magnetic center fragments beforehand. This procedure is well-described and implemented in the POLY_ANISO mod-

DOI: 10.1021/acs.inorgchem.5b01673
Inorg. Chem. 2015, 54, 11247−11258

ule.[46,48−50] One core feature of the Lines model to bear in mind is that it becomes exact in the case of two Ising-type ions (strong axial magnetization). With the resulting wave function for the dinuclear complex the magnetic susceptibility from dc-SQUID data can be simulated (see Figure 10). The only parameters are the exchange coupling constant J and a parameter zJ, which accounts for intermolecular interactions in the powder by a mean-field approach.

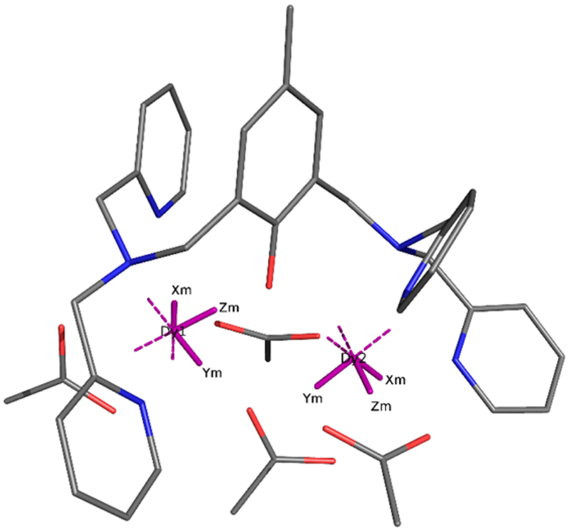

Figure 9. Orientation of the ab initio calculated main magnetic axes of the ground state Kramer doublets of $[\mathrm{Dy^{III}}_2(\mathrm{L})(\mathrm{OAc})_4]^+$ on the magnetic centers Dy1 (left) and Dy2 (right).

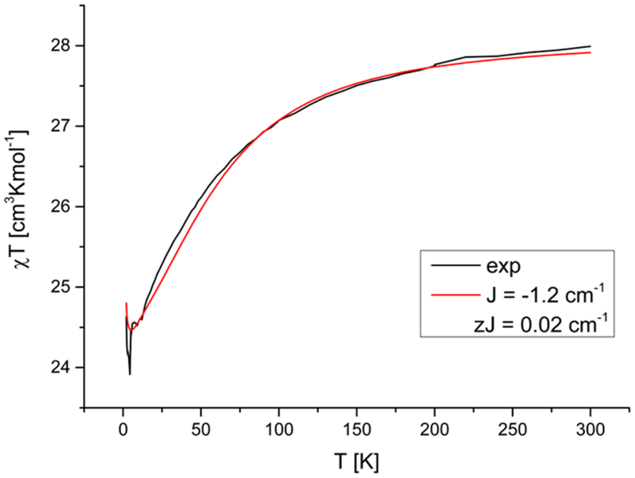

Figure 10. Black: Measured χT vs T data of $[\mathrm{Dy^{III}}_2(\mathrm{L})(\mathrm{OAc})_4]^+$. Red: Simulation of the χT vs T data on the basis of the ab initio calculated wave function with the exchange coupling constant $J = -1.2$ cm^{-1} and the parameter $zJ = -0.02$ cm^{-1}, to account for intermolecular coupling in the measured powder.

The directions of the local anisotropy axes for the dinuclear $\mathrm{Dy^{III}}$ complex are shown in Figure 9; the computed parameters are given in Table 2. This indicates that the local axes do not align, resulting in an easy plane and not an easy axis for the overall anisotropy of the complex. The simulation of the experimental χT versus T data yields an energy spectrum of the four lowest exchange states (Figure 11). The overall height of the potential is very low. Especially, the energy gap between the first excited exchange state and the ground state is less than a wavenumber. The fast relaxation exhibited by the dinuclear $\mathrm{Dy^{III}}$ complex, as seen in the experimental magnetic data indicates a very low blocking barrier, which is well-reproduced by the computational results, and this also emerges from the computed exchange spectrum given in Figure 11.

Apart from the noncolinearity of the local magnetic moments on the $\mathrm{Dy^{III}}$ centers, the nonaxiality of the ligand field proves to be an equally big problem. This becomes evident when looking at the ligand field in terms of the extended Stevens operators (see Supporting Information).[25] Since the system has C_1-symmetry no main quantization axis by standard convention can be given. The standard interpretation of the ESO parameters remains intact, even in nonaxial systems, but a total of 27 parameters are needed to describe the exact energy splitting. The z-axis was chosen to align with the orientation of the magnetic moment of the ground state Kramers doublet (Zm, see Figure 9). The axiality of the ground state KD (see Table 2 KD1(g_x, g_y, g_z)) is due to the perturbation by a close ligand atom. The B_n^0-values for the Dy2 center are all negative. This is the result of the axial component of the ligand field being stronger than the equatorial one; a strong axiality is needed to stabilize the $M_J = \pm 15/2$ state.[12] Especially, the Dy1 center shows an odd term B_2^1 which is non-negligible and points to a rather weak axiality of the system. The two $\mathrm{Dy^{III}}$ ions experience a vastly different ligand field, which is evident in the disjoined local anisotropy axes. This strengthens the belief that lanthanides are not that inert to ligand field effects as usually assumed and emphasizes the importance of a strongly axial ligand field.[51] Without a strong axiality of the ground and several excited Kramers doublets, one will always observe a very fast relaxation of one magnetic center, because of the possibility of reversal of magnetization by quantum tunneling (QTM) and Orbach or Raman relaxation pathways. Tunneling comes more into effect as the g_x and g_y components increase.[52] There are indications that the deviation of the orientation of the magnetic moments of the ground state Kramers doublet to the excited ones plays a major part in supporting spin−phonon relaxation pathways.[53] As of now there is no method to quantify the three possible relaxation pathways (thermal, QTM, Orbach), but a qualitative insight can be gained by the transition magnetic moment connecting the respective states (Figure 11).[54] This leads to the requirements that have to be met by a Dy-based SMM. A strong axial ligand field that leads to an energy separation of the ground state and excited state Kramers doublet by at least 100 cm^{-1}, a g_x, g_y < 0.2 and g_z > 18 and a colinearity of the orientation of magnetic axes between the ground and excited state Kramer doublets.

■ CONCLUSION

A large range of experimental and computational methods have been applied to a complete series of isostructural dinuclear lanthanide complexes. The ligand field analysis and ab initio calculations of the $\mathrm{Dy^{III}}_2$ complex are in excellent agreement with the experimental results, and the quantum-chemical calculations provide a good understanding of the fundamental reasons for the fast relaxation. The weak antiferromagnetic coupling of the $\mathrm{Dy^{III}}$ ions and the ill-matched local anisotropy, due to variations in local ligand fields, are the main reasons for the relaxation pathways. The results show a strong anisotropy but a very small barrier, leading to fast relaxation of magnetization. This highlights the importance of the coordination geometry, when designing small lanthanide-based SMMs. Although spin−orbit effects are of a much larger

Table 2. Energies and g-Tensor Components of the RASSI-SO Coupled Eight Kramers Doublets of the Dy^{III} Ground State Multiplet[a]

	E [cm^{-1}]					∠KD1–Dy–KDX [deg]	
Kramers doublets	Dy1	Dy2		Dy1	Dy2	Dy1	Dy2
1	0.000	0.000	g_x	0.0513	0.1523		
			g_y	0.0807	0.1785		
			g_z	19.6774	19.5093		
2	82.678	47.380	g_x	0.0105	0.1085	81.3	47.8
			g_y	0.2256	0.2098		
			g_z	17.9927	19.3994		
3	126.352	101.130	g_x	1.0239	2.2305	133.7	17.5
			g_y	2.1238	3.2754		
			g_z	14.5144	13.0475		
4	168.99	135.012	g_x	2.3042	9.5218	85.9	23.5
			g_y	3.6608	8.1274		
			g_z	12.5689	2.3023		
5	190.307	190.559	g_x	2.4158	1.6465	84.1	68.3
			g_y	5.6653	3.9979		
			g_z	9.1808	10.9756		
6	244.019	227.811	g_x	1.9934	1.8470	96.3	80.5
			g_y	2.8726	5.7434		
			g_z	13.4074	10.9760		
7	292.388	250.966	g_x	0.4709	0.9296	101.3	98.0
			g_y	0.5829	1.9883		
			g_z	18.5805	15.3747		
8	505.778	308.520	g_x	0.0087	0.2281	58.8	83.7
			g_y	0.0115	0.6409		
			g_z	19.7885	18.2012		

[a] The angle KD1–Dy–KDX gives the deviation of the main magnetic axis of each excited Kramers doublet with respect to the ground state KD1.

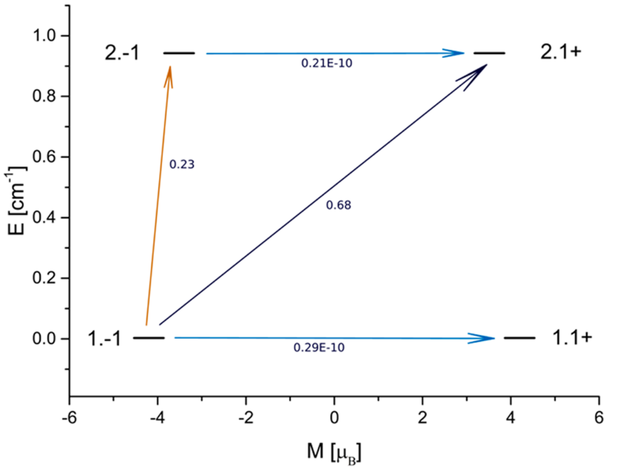

Figure 11. Ab initio calculated exchange spectrum of [Dy$^{III}_2$(L)(OAc)$_4$]$^+$ with four basis functions per magnetic center; the numbers at each arrow indicate the mean average matrix elements [$(|\mu_x| + |\mu_y| + |\mu_z|)/3$] connecting the stationary points to give a qualitative idea of the most probable relaxation pathway. Tunelling bewteen respective states is expected to be relevant above a factor of approximately 10^{-3}.

dimension, the energy barriers for relaxation are very small, and the small ligand field contributions therefore play a crucial role as well.

The important result of the present study is that the ab initio analysis used leads to excellent agreement with the experimental data and therefore allows for a thorough understanding of the relaxation pathways. Importantly, this will now allow us to predict the SMM behavior of this type of complexes, provided the structures of the complexes are known.

■ EXPERIMENTAL SECTION

Measurements. *Magnetic Measurements.* Magnetic measurements were carried out on a MPMS-XL 5T (Quantum Design) SQUID magnetometer. Samples were powdered and pressed in PTFE tape to avoid field-induced orientation. Data were corrected for diamagnetism of the sample holder, and Pascal's constants were used for diamagnetic corrections of the sample. Dynamic magnetic ac SQUID measurements were performed with a Quantum Design MPMS-XL7 SQUID. Polycrystalline samples were embedded in vaseline to prevent torqueing.

High-Frequency Electron Paramagnetic Resonance (HF-EPR). These measurements were performed on a powder sample of the dinuclear Gd^{III} complex in the frequency range ν = 32–330 GHz, and in a temperature range from 4 to 150 K. A millimeter vector network analyzer (MVNA) was used as a source and detector of stable microwave, and a superconducting magnet was applied to provide a magnetic field up to 15 T.[55]

Magnetic Circular Dichroism (MCD). Spectra were obtained in the range 350–1400 nm using a Jobin Yvon 750s monochromator with a Hinds photoelastic modulator to generate the circularly polarized modulation with either a Si-avalanche photodiode or an InGaAs detector for the visible and near-IR regions, respectively. The signals were acquired with Stanford SR830 lock-in amplifiers at chopped and circularly polarized modulations allowing the simultaneous measurement of absorption and MCD spectra. The sample was held in a 5 Telsa magnetic field of an Oxford SM-4 Spectramag at temperatures 2–10 K using an Oxford ITC504 controller. The MCD spectrum was calibrated using Co(en)$_3^{3+}$ as a standard for circular dichroism.[56]

X-ray Crystal Structure Determinations. Crystal data and details of structure determinations are given in the Supporting Information. CIF files for [$Y_2L(OAc)_4$]PF_6, [$Gd_2L(OAc)_4$]PF_6, [$Tb_2L(OAc)_4$]PF_6, [$Dy_2L(OAc)_4$]PF_6, [$Ho_2L(OAc)_4$]PF_6, [$Er_2L(OAc)_4$]PF_6 and [Lu$_2$L-

$(OAc)_4]PF_6$ are available as Supporting Information. CCDC files contain the crystallographic data of the structures reported here. These data can be obtained free of charge from The Cambridge Crystallographic Data Centre via www.ccdc.cam.ac.uk/data_request/cif.

Elemental analyses were obtained from the microanalytical laboratory of the Chemical Institutes of the University of Heidelberg.

Syntheses. *General.* Chemicals were used as supplied. Technical grade solvents were distilled prior to use. The ligand L (2,6-bis((bis(pyridin-2-ylmethyl)amino)methyl)-4-methylphenolate) was prepared as described.[57,58]

General Procedure for $[Ln_2(L)(OAc)_4]PF_6$. To a solution of L (200 mg, 0.4 mmol) in methanol (15 mL) was added a solution of $Ln(OAc)_3$ (0.8 mmol) in methanol/water (1:1, 10 mL). The solution was stirred at 55 °C for 1 h. NH_4PF_6 (160 mg, 1 mmol) was added, and the solution was stirred for an additional 30 min and was then left for evaporation in air.

$[Y_2(L)(OAc)_4]PF_6$. After 1 day, colorless crystals suitable for X-ray diffraction were obtained. Anal. Calcd for $[Y_2(L)(OAc)_4]PF_6 \cdot H_2O$ (%): C, 44.50; H, 4.28; N, 7.59. Found: C, 44.30; H, 4.21; N, 7.70. HR ESI-MS m/z: 915.1439 ($[Y_2(L)(OAc)_3(OMe)]^+$).

$[Nd_2(L)(OAc)_4]PF_6$. After 1 day, yellow crystals suitable for X-ray diffraction were obtained. Anal. Calcd for $[Gd_2(L)(OAc)_4]PF_6$ (%): C, 40.06; H, 4.02; N, 6.84. Found: C, 39.38; H, 4.42; N, 10.55. HR ESI-MS m/z: 1080.1789; calcd 1080.1724 ($[Gd_2L(OAc)_4]^+$).

$[Gd_2(L)(OAc)_4]PF_6$. After 1 day, yellow crystals suitable for X-ray diffraction were obtained. Anal. Calcd for $[Gd_2(L)(OAc)_4]PF_6$ (%): C, 40.06; H, 4.02; N, 6.84. Found: C, 40.31; H, 3.94; N, 6.65. HR ESI-MS m/z: 1080.1789; calcd 1080.1724 ($[Gd_2(L)(OAc)_4]^+$).

$[Tb_2(L)(OAc)_4]PF_6$. After 1 day, yellow crystals suitable for X-ray diffraction were obtained. Anal. Calcd for $[Tb_2(L)(OAc)_4]PF_6$ (%): C, 40.08; H, 3.69; N, 6.84. Found: C, 39.84; H, 3.94; N, 6.96. HR ESI-MS m/z: 1083.1772; calcd 1083.1750 ($[Tb_2(L)(OAc)_4]^+$).

$[Dy_2(L)(OAc)_4]PF_6$. After 1 day, yellow crystals suitable for X-ray diffraction were obtained. Anal. Calcd for $[Dy_2(L)(OAc)_4]PF_6$ (%): C, 39.85; H, 3.67; N, 6.46. Found: C, 39.62; H, 3.71; N, 6.46. HR ESI-MS m/z: 1090.1859; calcd 1090.1804 ($[Dy_2(L)(OAc)_4]^+$).

$[Ho_2(L)(OAc)_4]PF_6$. After 1 day, red crystals suitable for X-ray diffraction were obtained. Anal. Calcd for $[Ho_2(L)(OAc)_4]PF_6 \cdot NH_4PF_6$ (%): C, 34.82; H, 4.18; N, 6.46. Found: C, 34.95; H, 4.05; N, 6.30. HR ESI-MS m/z: 1027.1885 ($[Ho_2(L)(OAc)_2(OH)(MeO)]^+$).

$[Er_2(L)(OAc)_4]PF_6$. After 1 day, red crystals suitable for X-ray diffraction were obtained. Anal. Calcd for $[Er_2(L)(OAc)_4]PF_6$ (%): C, 39.54; H, 3.64; N, 6.75. Found: C, 39.65; H, 3.70; N, 6.62. HR ESI-MS m/z: 1055.1825 ($[Er_2(L)(OAc)_3(OH)]^+$).

$[Lu_2(L)(OAc)_4]PF_6$. After 1 day colorless crystals suitable for X-ray diffraction were obtained. Anal. Calcd for $[Lu_2(L)(OAc)_4]PF_6 \cdot 2NH_4PF_6$ (%): C, 30.96; H, 3.61; N, 7.04. Found: C, 30.45; H, 3.56; N, 7.02. HR ESI-MS m/z: 1087.2141 ($[Lu_2(L)(OAc)_3(OMe)]^+$).

■ ASSOCIATED CONTENT

Ⓢ Supporting Information

The Supporting Information is available free of charge on the ACS Publications website at DOI: 10.1021/acs.inorgchem.5b01673.

Crystallographic data (CIF)

Details of the crystallographic experiments, the complete list of magnetic data, details of the ligand field analysis, the MCD data, and quantum-chemical analysis (PDF)

■ AUTHOR INFORMATION

Corresponding Author

*E-mail: peter.comba@aci.uni-heidelberg.de. Fax: +49-6221-546617.

Notes

The authors declare no competing financial interest.

■ ACKNOWLEDGMENTS

Financial support by the German Science Foundation (DFG), the Deutscher Akademischer Austauschdienst (DAAD), the Graduate School HGS MathComp of the IWR, and the University of Heidelberg are gratefully acknowledged.

■ REFERENCES

(1) Caneschi, A.; Gatteschi, D.; Sessoli, R.; Barra, A. L.; Brunel, L. C.; Guillot, M. *J. Am. Chem. Soc.* **1991**, *113*, 5873−5874.

(2) Sessoli, R.; Tsai, H.-L.; Schake, A. R.; Wang, S.; Vincent, J. B.; Folting, K.; Gatteschi, D.; Christou, G.; Hendrickson, D. N. *J. Am. Chem. Soc.* **1993**, *115*, 1804−1816.

(3) Sessoli, R.; Gatteschi, D.; Caneschi, A.; Novak, M. A. *Nature* **1993**, *365*, 141−143.

(4) Arom, G.; Aubin, S. M. J.; Bolcar, M. A.; Christou, G.; Eppley, H. J.; Folting, K.; Hendrickson, D. N.; Huffman, J. C.; Squire, R. C.; Tsai, H.-L.; Wang, S.; Wemple, M. W. *Polyhedron* **1998**, *17*, 3005−3020.

(5) Gatteschi, D.; Sessoli, R. *Angew. Chem., Int. Ed.* **2003**, *42*, 268−297.

(6) Long, J. R. Molecular Cluster Magnets. In *Molecular Cluster Magnets in Chemistry of Nanostructured Materials*; Yang, P., Ed.; World Scientific: Hong Kong, 2003; pp 291−315.

(7) Glaser, T. *Chem. Commun.* **2011**, *47*, 116−130.

(8) Atanasov, M.; Comba, P.; Hausberg, S.; Martin, B. *Coord. Chem. Rev.* **2009**, *253*, 2306−2314.

(9) Neese, F.; Pantazis, D. A. *Faraday Discuss.* **2011**, *148*, 229−238.

(10) Comba, P.; Kerscher, M. *Coord. Chem. Rev.* **2009**, *253*, 564−574.

(11) Aromi, G.; Brechin, E. K. In *Struct. Bonding (Berlin)*; Springer-Verlag: Berlin, 2006; Vol. *122*, pp 1−67.

(12) Rinehart, J. D.; Long, J. R. *Chem. Sci.* **2011**, *2*, 2078−2085.

(13) Sorace, L.; Benelli, C.; Gatteschi, D. *Chem. Soc. Rev.* **2011**, *40*, 3092−3104.

(14) Guo, Y.-N.; Xu, G.-F.; Guo, Y.; Tang, J. *Dalton Trans.* **2011**, *40*, 9953−9963.

(15) Hoeke, V.; Stammler, A.; Bögge, H.; Schnack, J.; Glaser, T. *Inorg. Chem.* **2014**, *53*, 257−268R.

(16) Sessoli, R.; Powell, A. K. *Coord. Chem. Rev.* **2009**, *253*, 2328−2341.

(17) Guo, Y.-N.; Chen, X.-H.; Xue, S.; Tang, J. *Inorg. Chem.* **2011**, *50*, 9705−9713.

(18) Ceulemans, A.; Chibotaru, L. F.; Heylen, G. A.; Pierloot, K.; Vanquickenborne, L. G. *Chem. Rev.* **2000**, *100*, 787−806.

(19) Chibotaru, L. F.; Ungur, L. *J. Chem. Phys.* **2012**, *137*, 064112-1−064112-22.

(20) Singh, S. K.; Rajaraman, G. *Chem. - Eur. J.* **2014**, *20*, 113−123.

(21) Atanasov, M.; Busche, C.; Comba, P.; El Hallak, F.; Martin, B.; Rajaraman, G.; van Slageren, J.; Wadepohl, H. *Inorg. Chem.* **2008**, *47*, 8112−8125.

(22) Atanasov, M.; Comba, P.; Helmle, S.; Müller, D.; Neese, F. *Inorg. Chem.* **2012**, *51*, 12324−12335.

(23) Malmqvist, P.-A.; Roos, B. O.; Schimmelpfennig, B. *Chem. Phys. Lett.* **2002**, *357*, 230−240.

(24) Lines, M. E. *J. Chem. Phys.* **1971**, *55*, 2977−2984.

(25) Rudowicz, C. *J. Phys. C: Solid State Phys.* **1985**, *18*, 1415−1430.

(26) Atanasov, M.; Comba, P.; Förster, S.; Linti, G.; Malcherek, T.; Miletich, R.; Prikhod'ko, A.; Wadepohl, H. *Inorg. Chem.* **2006**, *45*, 7722−7735.

(27) Miyashita, Y.; Sanada, M.; Islam, M. M.; Amir, N.; Koyano, T.; Ikeda, H.; Fujisawa, K.; Okamoto, K. *Inorg. Chem. Commun.* **2005**, *8*, 785−788.

(28) Li, Y.; Zheng, F.-K.; Liu, X.; Zou, W.-Q.; Guo, G.-C.; Lu, C.-Z.; Huang, J.-S. *Inorg. Chem.* **2006**, *45*, 6308−6316.

(29) Niu, S. Y.; Jin, J.; Jin, X. L.; Yang, Z. Z. *Solid State Sci.* **2002**, *4*, 1103−1106.

(30) Costes, J.-P.; Dahan, F.; Dupuis, A.; Lagrave, S.; Laurent, J.-P. *Inorg. Chem.* **1998**, *37*, 153−155.

(31) Luis, F.; Bartolome, J.; Fernandez, J. F.; Tejada, J.; Hernandez, J. M.; Zhang, X. X.; Ziolo, R. *Phys. Rev. B: Condens. Matter Mater. Phys.* **1997**, *55*, 11448−11456.

(32) Abragam, A.; Bleaney, B. *Electron Paramagnetic Resonance of transition Ions*; Clarendon Press: Oxford, 1970.

(33) An easy plane-type system can also have a maximal absorption appearing in the lower field region of the resonance at low temperature. However, the simulation of ZFS induced by the magnetic dipolar coupling for an easy plane-type system with $g \sim 2.01$ yields 2.5 GHz, which is not confirmed by the experimental results.

(34) Benchini, A.; Gatteschi, D. *EPR of Exchange Coupled Systems*; Dover: Mineola, NY, 2012.

(35) Smith, T. D.; Pilbrow, J. R. *Coord. Chem. Rev.* **1974**, *13*, 173−278.

(36) Baggio, R.; Calvo, R.; Garland, M. T.; Pena, O.; Perec, M.; Rizzi, A. *Inorg. Chem.* **2005**, *44*, 8979−8987.

(37) Yeung, Y.-Y.; Tanner, P. A. *J. Alloys Compd.* **2013**, *575*, 54−60.

(38) Rana, R. S.; Shertzer, J.; Kaseta, F. W.; Garvey, R.; Rana, D.; Feng, S. Y. *J. Chem. Phys.* **1988**, *88*, 2242−2248.

(39) Görller-Walrand, C.; Binnemans, K. In *Handbook on the Physics and Chemistry of Rare Earths*; Gschneidner, K. A., Eyring, L., Eds.; Elsevier: New York, 1996; Vol. *23*, pp 121−283.

(40) Wybourne, B. G. *Spectroscopic Properties of Rare Earths*; Interscience: New York, 1965.

(41) Judd, B. R. *Operator Techniques in Atomic Spectroscopy*; University Press: Princeton, NJ, 1998.

(42) Gerloch, M.; McMeeking, R. F. *J. Chem. Soc., Dalton Trans.* **1975**, 2443−2451.

(43) Görller-Walrand, C.; Binnemans, K. Spectral Intensities of f-f Transitions. In *Handbook on the Physics and Chemistry of Rare Earths*; Gschneidner, K. A., Eyring, L., Ed.; Elsevier: New York, 1998; Vol. 25, pp 101−264.

(44) Aquilante, F.; De Vico, L.; Ferré, N.; Ghigo, G.; Malmqvist, P.-A.; Neogrády, P.; Pedersen, T. B.; Pitonak, M.; Reiher, M.; Roos, B. O.; Serrano-Andrés, L.; Urban, M.; Veryazov, V.; Lindh, R. *J. Comput. Chem.* **2010**, *31*, 224−247.

(45) Roos, B. O.; Lindh, R.; Malmqvist, P.-A.; Veryazov, V.; Widmark, P.-O. *J. Phys. Chem. A* **2005**, *109*, 6575−6579.

(46) Ungur, L.; Van den Heuvel, W.; Chibotaru, L. F. *New J. Chem.* **2009**, *33*, 1224−1230.

(47) Roos, B. O.; Taylor, P. R.; Siegbahn, P. E. M. *Chem. Phys.* **1980**, *48*, 157−173.

(48) Chibotaru, L. F.; Ungur, L.; Soncini, A. *Angew. Chem., Int. Ed.* **2008**, *47*, 4126−4129.

(49) Chibotaru, L. F.; Ungur, L.; Aronica, C.; Elmoll, H.; Pilet, G.; Luneau, D. *J. Am. Chem. Soc.* **2008**, *130*, 12445−12455.

(50) Ungur, L.; Chibotaru, L. F.; Thewissen, M.; Costes, J.-P.; Wernsdorfer, W. *Inorg. Chem.* **2013**, *52*, 6328−6337.

(51) Ungur, L.; Chibotaru, L. F. *Phys. Chem. Chem. Phys.* **2011**, *13*, 20086−20090.

(52) Friedman, J. R.; Sarachik, M.; Tejada, J.; Ziolo, R. *Phys. Rev. Lett.* **1996**, *76*, 3830−3833.

(53) Leuenberger, M. N.; Loss, D. *Phys. Rev. B: Condens. Matter Mater. Phys.* **2000**, *61*, 1286−1302.

(54) Ungur, L.; Le Roy, J. J.; Korobkov, I.; Murugesu, M.; Chibotaru, L. F. *Angew. Chem., Int. Ed.* **2014**, *53*, 4413−4417.

(55) Golze, C.; Alfonsov, A.; Klingeler, R.; Büchner, B.; Kataev, V.; Mennerich, C.; Klauss, H.-H.; Goiran, M.; Broto, J.-M.; Rakoto, H.; Demeshko, S.; Leibeling, G.; Meyer, F. *Phys. Rev. B: Condens. Matter Mater. Phys.* **2006**, *73*, 224403-1−224403-8.

(56) McCaffery, A. J.; Mason, S. F. *Mol. Phys.* **1963**, *6*, 359−371.

(57) Suzuki, M.; Kanatomi, H.; Murase, I. *Chem. Lett.* **1981**, *10*, 1745−1748.

(58) Borovik, A. S.; Papaefthymiou, V.; Taylor, L. F.; Anderson, O. P.; Que, L. *J. Am. Chem. Soc.* **1989**, *111*, 6183−6195.

DOI: 10.1021/acs.inorgchem.5b01673
Inorg. Chem. 2015, 54, 11247−11258